

IPTC-22131-MS

Segmentation of X-Ray Images of Rocks Using Supervoxels Over-Segmentation

Hussain Alqahtani, Naif Alqahtani, Ryan T. Armstrong, and Peyman Mostaghimi, University of New South Wales

Copyright 2022, International Petroleum Technology Conference DOI [10.2523/IPTC-22131-MS](https://doi.org/10.2523/IPTC-22131-MS)

This paper was prepared for presentation at the International Petroleum Technology Conference held in Riyadh, Saudi Arabia, 21-23 February 2022.

This paper was selected for presentation by an IPTC Programme Committee following review of information contained in an abstract submitted by the author(s). Contents of the paper, as presented, have not been reviewed by the International Petroleum Technology Conference and are subject to correction by the author(s). The material, as presented, does not necessarily reflect any position of the International Petroleum Technology Conference, its officers, or members. Papers presented at IPTC are subject to publication review by Sponsor Society Committees of IPTC. Electronic reproduction, distribution, or storage of any part of this paper for commercial purposes without the written consent of the International Petroleum Technology Conference is prohibited. Permission to reproduce in print is restricted to an abstract of not more than 300 words; illustrations may not be copied. The abstract must contain conspicuous acknowledgment of where and by whom the paper was presented. Write Librarian, IPTC, P.O. Box 833836, Richardson, TX 75083-3836, U.S.A., fax +1-972-952-9435.

Abstract

Digital core analysis has gained the interest of many scientific communities because of its impact on our understanding of flow in porous media. A typical workflow in digital core analysis includes scanning, reconstruction, denoising, segmentation, and modeling. Image analysis and modeling highly depend on the quality of the segmentation step. In this regard, conventional image segmentation methods often require user input/interference. This results in user bias and may produce a range of possible segmentation outcomes. To address this, we propose an unsupervised machine learning framework that offers multiple functionalities including improved mineral and micro-porosity identification. Superpixel (2D) and (3D) work by over-segmenting greyscale images using a family of over-segmentation algorithms. Simple Linear Iterative Clustering (SLIC) is one of these algorithms that is recognized for its speed and memory efficiency. The proposed framework utilizes SLIC and unsupervised clustering methods for segmenting greyscale images. SLIC divides the 2D and 3D images into segments having pixels (or voxels) with similar features (i.e., intensity range). Statistical features of each segment are computed and used for identifying the segment label through unsupervised clustering techniques. The unsupervised voting clustering implements a majority voting policy from multiple clustering algorithms including Hierarchical clustering and k-means clustering. A North Sea sandstone 2D X-ray image along with its SEM image were used to validate this framework. Different metrics were used to measure the accuracy of the X-ray segmentation with SEM segmentation. Our results show a mean Jaccard index of 70% and a mean Dice index of 81%. The same workflow is applied using supervoxels on a high-resolution 3D Indiana Limestone image and the results show similar accuracy margins compared to watershed segmentation. Comparison with other segmentation methods shows an average Jaccard score of 74% and an average Dice index score of 83%. To the best of our knowledge, this is the first application of superpixels over-segmentation algorithms in semantic segmentation of X-ray micro-CT images of porous media. The findings of this study highlighted the advantage of these algorithms in detecting sub-resolution porosity regions in greyscale images and obtaining accurate multi-label segmentation.

Introduction

In recent years, digital core analysis has expanded our knowledge of many topics related to flow in porous media. Its use in the oil and gas industry is of high importance as it is beneficial for the petrophysical characterization of core samples (Ketcham & Carlson, 2001). It can be used to analyze the structure, composition, grain shapes, pore network, and heterogeneity of core samples. A reliable qualitative and quantitative analysis of rock images can be used for cross-correlation of rock properties from pore to core scales (Grachev, 2012). A typical workflow for digital core analysis is as follows. First, the core is scanned using a micro-CT scanner, then the acquired X-ray projections are reconstructed to create a 3D volumetric image. The image is processed by removing imaging artifacts such as dead pixels, ring artifacts, or beam hardening. The processed image is a greyscale image that must be segmented to assign a phase for each voxel and identify the pore space. Once the 3D image is segmented, it will be used for numerical simulation of flow within the pores to predict the effective properties of the core samples (Blunt et al., 2013; Mostaghimi et al., 2017).

Conventional image segmentation techniques such as thresholding, or region-based methods are user biased. Discrepancies in these outcomes strongly affect all subsequent petrophysical analyses (Niu et al., 2020). A common approach in segmentation is binarization where two phases are identified to distinguish between pore space and the solid matrix (minerals). However, there is no specific framework or methodology in the literature for the identification of micro-porous regions, that is pores that are below the image resolution, other than choosing thresholds. This paper will address these issues by providing an unsupervised machine learning framework to segment and characterize micro-porosity in heterogeneous samples.

Many researchers evaluated different segmentation methods on pore-scale images. One of the main segmentation methods is global thresholding methods. In global thresholding methods, a grayscale value is defined to separate the image into two regions of interest based on the image's gray value histogram (Vogel & Kretzschmar, 1996). As an extension to the global thresholding methods, Oh & Brent Lindquist (1999) developed an Indicator Kriging-based segmentation method to incorporate spatial information into the segmentation process. However, the Kriging-based segmentation method still depends on the user choice of threshold values and requires *a-priori* partial identification of some of the image. Later, Sheppard et al. (2004) proposed an anisotropic diffusion filter for smoothing the image, and then an unsharp mask to enhance the edges of the image, followed by a combination of watershed transform and a modified region-based segmentation method using active contours. Such methods still require a degree of user interference in the filtering processes and the tuning of parameters making the process susceptible to user bias (Malik et al., 2018). One of the common automatic thresholding methods was suggested by Otsu (1979) to automatically select a threshold or a set of thresholds from different classes. However, Otsu's method does not take local spatial information into consideration (Hapca et al., 2013). As an enhancement to Otsu's method, Hapca et al. (2013) proposed a pre-classification step on the solid phase to be performed before thresholding to consider the heterogeneity of the solid phase. However, this preclassification step is computationally demanding, especially for larger images ($> 1000^3$ voxels) (Hapca et al., 2013). To test the aforementioned segmentation methods, Wang et al. (2011) generated eight 2D binary soil images to be used as the ground truth. Then, they tested the performance of multiple segmentation algorithms and compared the results with the ground truth binary image. Indicator kriging segmentation outperformed all other segmentation methods. The results of the study indicate how the choice of the threshold value is dependent on the user choice which may lead to misclassification of pore and solid labeling. Recently, machine learning algorithms have been utilized in digital rock physics. These algorithms are useful in feature extraction, image processing, and segmentation (Cortina-Januchs et al., 2011). In an application of machine learning methods, Cortina-Januchs et al. (2011) used a novel approach to detect pore space in micro-CT images of soil by using image processing, data clustering, and ANN algorithms. They used an artificial neural network (ANN) as a classifier to detect pore

space in the images and the results were matching the results from the clustering segmentation algorithms. Later, [Chauhan et al. \(2016\)](#) tested seven machine learning algorithms namely k-means, fuzzy c-means, self-organized maps, feed-forward artificial neural networks, least-square support vector machine, bagging, and boosting to segment and calculate the porosity of an Andesite rock sample. All of these algorithms showed reasonable accuracy in porosity calculations compared to experimental data.

Sub-resolution porosity, sometimes referred to as micro-porosity, is one of the challenges in digital rock physics. The term refers to pore space below the imaging voxel size which cannot be resolved using micro-CT. Microporous regions identification is useful for descriptive analysis of flow behavior and transport phenomena in the pore space ([Lin et al., 2016](#)). The identification of micro-porosity often requires combining micro-CT imaging with Scanning Electron Microscope (SEM) imaging ([Smith et al., 2013](#)). To detect micro-porosity without the need to acquire SEM images, [Lin et al. \(2016\)](#) suggested a differential imaging technique that involves flooding the core with high salinity brine. This technique provides images with higher contrast that help in identifying low-density minerals in the solid phase to avoid misclassification ([Lin et al., 2016](#)). Nevertheless, this method requires time-consuming steps (i.e. flooding the core, multiple scans, and processing).

In addition, over-segmentation or superpixel methods are used to divide a region of one object into a large number of fragments. These fragments are generated based on their inner similarities or their discontinuity at the borders of other regions. Similarity and discontinuity are assessed based on different parameters such as grey-level intensity, textural analysis, spatial information, and color ([Neubert, 2015](#)). Generally, over-segmentation methods can be divided into graph-based methods, energy-based methods, and clustering-based methods ([Neubert, 2015](#)). Their main applications are in object detection and spatial statistics recognition. A few examples of object recognition superpixel-based algorithms are Selective Search ([Uijlings et al., 2013](#)) or Multiscale Combinatorial Grouping ([Pont-Tuset et al., 2015](#)). Also, superpixel methods can be used for semantic segmentation purposes ([Mičušík & Košecká, 2009](#)) or 3D reconstruction from single views ([Hoiem et al., 2005](#)). Over years of research on superpixel algorithms, many methods have been developed, starting with the very first superpixel algorithm Normalized Cuts (NC) developed by [Shi & Malik \(2000\)](#). They proposed a graph-based solution to the eigenvalue problem on the image graph seeking optimization in total dissimilarity between segments and similarity within each segment. Their first code was able to produce a few large segments. Later, they utilized their algorithm as a pre-processing step to merge smaller similar pixels segments. After that, [Comaniciu & Meer \(2002\)](#) proposed an Edge Augmented Mean Shift (EAMS) algorithm that is based on mean shift segmentation and edge detection techniques.

In this paper, we address the abovementioned issues of user-biased segmentation by providing a machine learning framework that minimizes human interference in the segmentation process and utilizes spatial and statistical information to cluster and segment 2D images or 3D volumes. The proposed framework is tested against ground truth segmentation of SEM image in the 2D application and a highresolution volume in the 3D application. The results demonstrate the potential of machine learning methods for fully automated digital rock analysis.

Materials and Methods

Materials. Two sets of images are considered in this study. First, a 2D X-ray image of a North Sea sandstone with its registered SEM image. Second, a 3D volume of Indiana limestone was used to assess the proposed framework in the 3D application. The details of all images are described in [Table 1](#).

Table 1—Samples used to establish the framework

Name	Resolution (μm)	Porosity	Size	Reference/Imaging Facility
North Sea Sandstone (X-ray)	2.30	20.429%	6100×6100	(Niu et al., 2020) / Australian National University
North Sea Sandstone (SEM)	0.50	20.429%	6100×6100	(Niu et al., 2020) / Australian National University
Indiana Limestone	5.30	10%	$1024 \times 1024 \times 1024$	(Alqahtani et al., 2021)/ University of New South Wales-Tyree X-ray

For the 2D application, X-ray and SEM images of the original North Sea sandstone (Niu et al., 2020; Scott, 2020) were segmented into three phases: pore, low-density minerals, and high-density minerals. Two methods were used to segment the X-ray images: (1) Otsu's segmentation (Otsu, 1979) thresholding using ImageJ software and (2) watershed-based method (Leu et al., 2014) using Avizo software. The SEM image was segmented using a watershed-based method (Leu et al., 2014) using Avizo software. For our analysis and comparison, the SEM segmentation will be used as the ground truth segmentation while the X-ray segmentation will be used for comparison only. For the 3D application, the original X-ray images of Indiana limestone (Alqahtani et al., 2021; Alqahtani et al., 2021) were segmented using watershed method using Avizo software aided by Mercury Injection Capillary Pressure (MICP) analysis for determining macro- and micro-pores. This segmentation will be used as the ground truth segmentation.

Segmentation workflow. The two major considerations in constructing this workflow are the image resolution impact on image segmentation and how to benefit from spatial information of a group of pixels/voxels instead of taking each pixel/voxel intensity value as a standalone value in image segmentation. The proposed framework is accomplished in four steps as shown in Figure 2. In brief, the first step is the initial image processing. The second step initiates the generation of superpixels/supervoxels. The third step involves superpixels/supervoxels features extraction. The fourth step applies three different unsupervised clustering techniques to cluster all generated superpixels/supervoxels and then establishes a majority voting clustering policy to assign a final label to each superpixel/supervoxel.

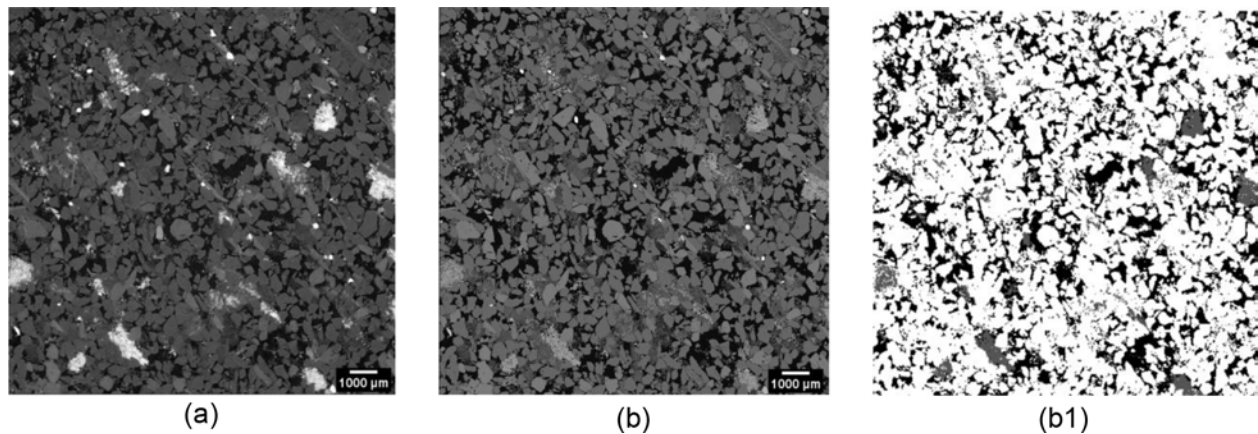


Figure 1—Materials used: (a) X-ray image of North Sea sandstone; (b) SEM image of North Sea Sandstone; (b1) WS segmentation of the SEM image (Ground Truth)

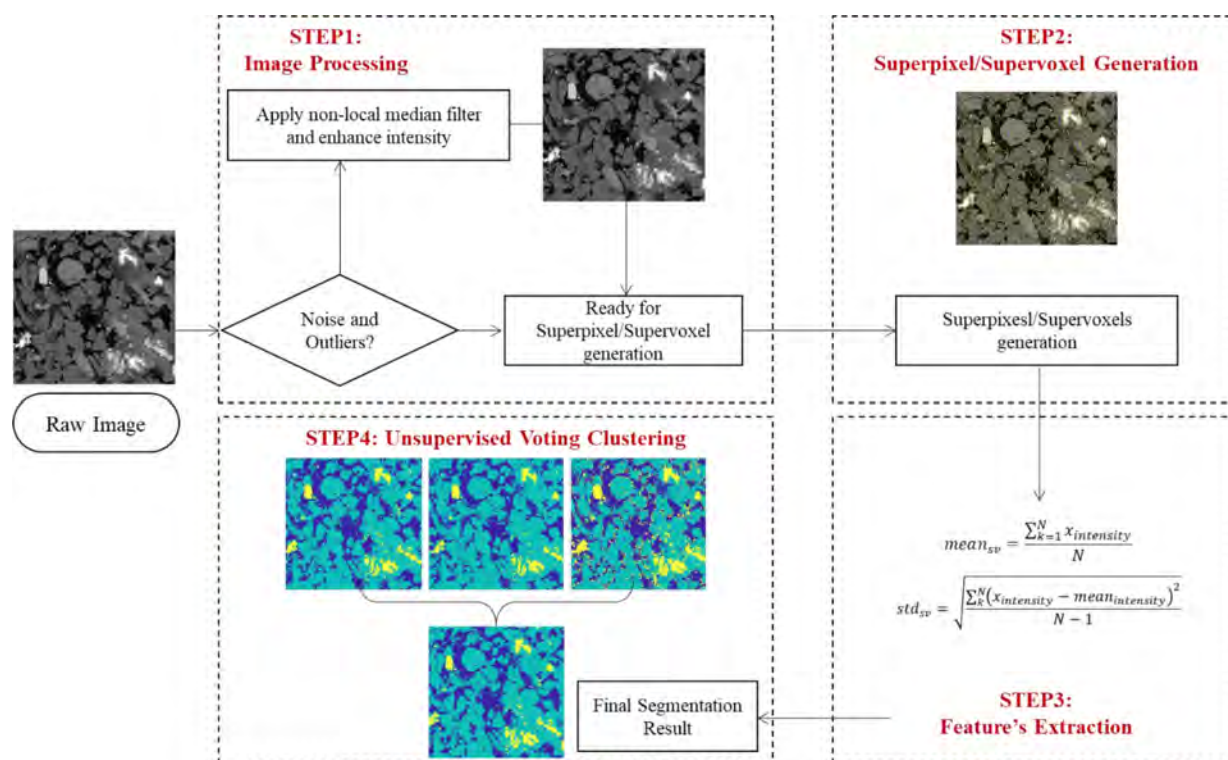


Figure 2—Illustration of our proposed workflow; STEP1: Image processing; STEP2: Utilizing SLIC algorithm to generate superpixels/supervoxels; STEP3: Extract Statistical features from every superpixel/supervoxel; STEP4: utilize three unsupervised clustering techniques and take the mode of each classification

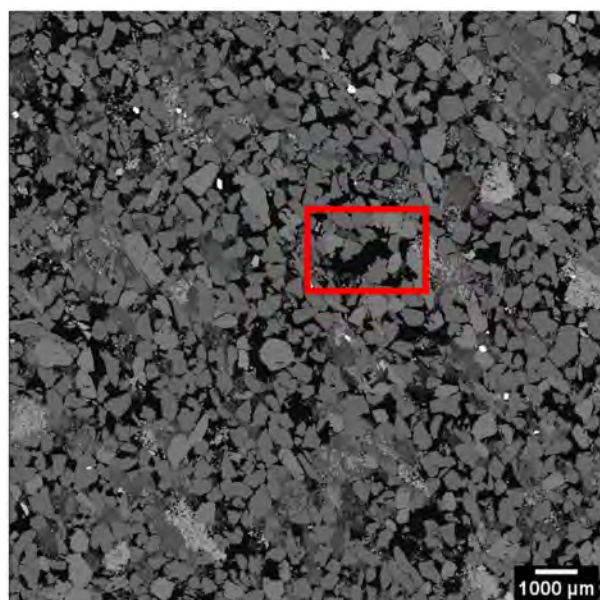


Figure 3—Showcase of missing grains in the SEM image

STEP 1: Image Processing. Scanning artifacts might affect or blur some of the features in images or change the CT value of certain material in different parts of an image (Ketcham & Carlson, 2001). Therefore, image processing is the first step that has to be done prior to any qualitative or quantitative analysis on a digital core image. The most occurring artifacts encountered for developing this workflow are image darkness and image noise. Thus, both artifacts and their remedial actions are discussed in this step. Sometimes, micro-CT images can be dark after acquisition. In such an instance, the greyscale histogram is skewed towards the low spectrum of intensity values. Thus, the intensity values have to be remapped

across the full range. This results in a brighter image while preserving all physical information of the image (Leu, 1992). The other artifact is image noise. Image noise is caused by an error in the statistical count of photons that results in the appearance of high-intensity elements that exist in certain pixels/voxels and the disappearance of low-intensity ones (Boas & Fleischmann, 2012). To resolve this issue, a median filter is applied (Pitas & Venetsanopoulos, 1986) on the image. Median filters are calculated by sliding a window of $M \times M$ pixels over the noisy image and replacing the center pixel value of that window with the median value of all pixels that exist in that window (Dinç et al., 2015). We find the application of the median filter aids the generation of more accurate superpixel boundaries.

STEP 2: Superpixels/Supervoxels Generation. While there are a variety of methods to generate superpixels, we opt to use Simpler Linear Iterative Clustering (SLIC) (Achanta et al., 2012). It has been shown to outperform other superpixel/supervoxel algorithms in memory efficiency, boundary adherence, speed, and application in segmentation algorithms (Achanta et al., 2012). SLIC generates superpixels/supervoxels by clustering pixels or voxels based on similarity and proximity in the image plane. The main user input in the algorithm is the desired number of segments k . Then, the algorithm starts clustering by an initialization step where the algorithm chooses a center of superpixel along the CIELAB color space $C_k = [I_k, a_k, b_k, x_k, y_k]^T$ where $k = [1, k]$ and starts sampling at regular grid space S pixels apart. To produce roughly equally sized superpixels, spacing should be

$$S=N/k$$

. It is worth noting that the algorithm chooses the centers of each superpixel at the lowest gradient descent in a 3×3 neighborhood to avoid centering the superpixels on edges or noisy parts of the image. The next step is the assignment, each pixel i in the image is associated with the nearest cluster center where the search area of pixel I is overlapping pixel i . In this step, SLIC is very optimized as the search area is $2S \times 2S$ compared to standard k -means search for the whole image. Once all pixels in the image are associated with their nearest clusters, a new center computation takes place to average all [labxy] vector of all pixels belonging to the cluster. A summary of SLIC algorithm is shown in Table 2.

Table 2—Summary of SLIC Algorithm (Achanta et al., 2010)

Algorithm 1 Efficient superpixel segmentation	
1:	Initialize cluster centers $C_k = [I_k, a_k, b_k, x_k, y_k]^T$ by sampling pixels at regular grid step S .
2:	Perturb cluster centers in an $n \times n$ neighbourhood, to the lowest gradient position.
3:	repeat
4:	foreach cluster center C_k do
5:	Assign the best matching pixels from a $2S \times 2S$ square neighbourhood around the cluster center according to the distance measure center
6:	end for
7:	Compute new cluster centers and residual error E {L1 distance between previous centers and recomputed centers}
8:	until $E \leq \text{threshold}$
9:	Enforce connectivity

STEP 3: Features' Extraction. For optimal classification and labeling, we extract statistical features from each superpixel/supervoxel. These features will allow quantifying specific discriminant information of each superpixel/supervoxel that will ease the process of classification in the upcoming step of the workflow. Each superpixel/supervoxel is used to extract the mean and the standard deviation of its corresponding intensity values,

$$\text{meansv} = \sum_{k=1}^N \text{intensity}_k / N \quad (1)$$

$$\text{stdsv} = \sqrt{\sum_{k=1}^N (\text{intensity}_k - \text{meanintensity})^2 / (N - 1)} \quad (2)$$

where N in eq (1) and eq (2) is the number of pixels/voxels in each superpixel/supervoxel.

STEP 3: Unsupervised Voting Clustering. Clustering can be defined as dividing a set of data into a different number of labeled groups based on a defining measure of dissimilarity or based on a recognized pattern structure from the data. Generally, clustering algorithms can be divided into two broad classifications: Non-Parametric Clustering and Parametric Clustering Methods (Olaode et al., 2014). In our proposed framework, we cluster the generated superpixels/supervoxels; based on their extracted features; utilizing two non-parametric clustering algorithms namely k -means clustering and an agglomerative approach of hierarchical clustering and a probabilistic parametric clustering method namely Gaussian Mixture Model (GMM).

k -means Clustering. In k -means algorithms, datasets are divided into k clusters into two-sequenced steps. The first step is the calculation of k number of centroids in the tested data. The second step is the assignment of every data point to its nearest specific centroid. The most common distance measure to the nearest centroid is Euclidian distance (Olaode et al., 2014). Each cluster is defined by its centroid and its constituent data points. Once clusters are defined, the algorithm recalculates the centroids of clusters in an iterative process to minimize the Euclidian distance between each cluster and its constituent data points until the squared root error function is minimum (Chauhan et al., 2016). For image segmentation purposes, k -means imposes a challenge in its random initial centroids' selection (Olaode et al., 2014).

Agglomerative Clustering. Hierarchical clustering algorithms build a hierarchy between clusters by considering the whole dataset as a cluster at the highest hierarchy while each data point is considered a cluster by itself at the lowest hierarchy (Olaode et al., 2014). Agglomerative clustering is an approach that starts from each datapoint/cluster and merges the similar data points into a newly defined cluster in a bottom-up approach. In our proposed framework, we use Ward's minimum variance method (Ward, 1963) as the similarity measure or the linkage between clusters. Ward's method minimizes the variance between datapoints in each defined cluster. In high-dimensional structural data, such as images, agglomerative clustering by itself might not be an efficient clustering algorithm as it looks for the similarity measure between clusters to be merged and does not look into the global similarities in the dataset (Demuth & Beale, 2000).

Gaussian Mixture Model Clustering. Gaussian Mixture Models (GMM) are a kind of statistical mixture model that represents a probabilistic model of a subpopulation within an overall population. Generally, mixture models have two sets of parameters: the mixing proportions and the parameters associated with each component distribution (Srivastava, 2007). In GMM, a single probability density function is fitted to the data to represent each sample with a vector of dimensions similar to the number of Gaussians in the mixture (Srivastava, 2007). The main disadvantage of GMMs is that they only provide good results when the distribution of data is known or can be estimated (Olaode et al., 2014).

Voting Clustering. Each clustering technique mentioned earlier is prone to errors and misclassification. To maximize the benefit and minimize the error of each clustering technique, we implemented a voting policy that takes the classification of each generated superpixel/supervoxel from the above algorithm and assigns the mode of the classifications to it. Results showed improvements when applying this technique.

Framework Validation

Segmentation Accuracy Metrics. To assess our framework, two segmentation metrics were used: intersection over union (IoU) metric which is also known as Jaccard index, and dice coefficient metric (DCM). Both metrics give a value of one as a maximum value when the two samples are the same and zero as a minimum value when the two samples are completely different. Considering two samples A and B,

$$IoU=A \cap B / A \cup B \quad (3)$$

$$I_0 U = A \cap B A \cup B \quad (3)$$

$$DCM=2 \times (A \cap B) A+B \quad (4)$$

Measurements of Physical Properties. Segmentation accuracy metrics by themselves could be misleading in the evaluation process. Thus, some physical parameters were obtained to assess the accuracy of the proposed framework: volume fractions, pore size distribution, and permeability for the 3D application. Volume fractions were calculated by counting the number of pixels/voxels of a phase to the total number of pixels/voxels. Porosity in this paper refers to the fraction of resolved pores. Pore size distribution was calculated using [Gostick et al. \(2019\)](#) open-source published code. Permeability was calculated along the X, Y, and Z directions of our 512³ Indiana Limestone sample using the method developed by [Chung et al. \(2019\)](#).

2D Application. We applied the framework to a subsection of the image of size 2000×2000 pixel. The reason for choosing a subsection of the image, and not the entire image, is that the ground truth image (SEM image) was missing some of the grains as shown in Figure 3. This is probably due to the polishing process for obtaining flat specimens for SEM imaging (Kjellsen et al., 2003). In addition, we wanted to choose a part of the image where all three phases coexist. Figure 4 shows the chosen section of the image along with its superpixel segmentation and the ground truth segmentation. To generate the superpixel segmentation, we divided the image into 40,000 segments that are equivalent to 1% of the image size in voxels. Each segment was utilized to extract its statistical features from the mean and the standard deviation of its intensities' values.



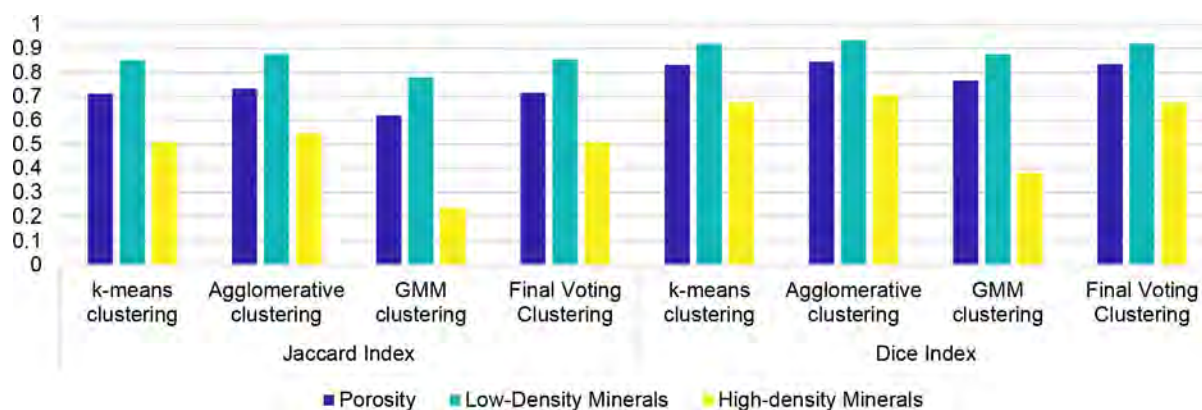


Figure 5—Summary of similarity indices results of 2D framework

Segmentation Metrics Accuracy Results. Superpixel segmentation resulted in an average Jaccard score of 70%, and an average Dice index score of 80%. Interestingly, it is noted that both metrics resulted in a low score for the high-density mineral phase. The reason behind such a low score is perhaps the unconformity of superpixel boundaries as we are using 1% of the total pixels count of the image to segment the image. Also, the constituents of each superpixel in the high-density mineral's region have higher mean values and higher-standard deviation values which forces the classification algorithm to assign a high-density label to that superpixel. In addition, the X-ray grayscale image has a lower resolution ($2.3 \mu\text{m}$) compared to the SEM image ($0.5 \mu\text{m}$). Therefore, such error margins can be justified.

On the other hand, comparing the classification algorithms, we find that agglomerative clustering outperforms all other classification algorithms while Gaussian Mixture Model clustering resulted in the lowest score of all indices. As explained earlier, GMM models need prior knowledge of the distribution of the data. In our case, once superpixels are generated, distribution of the data is dependent on the number of generated superpixels. Figure 5 summarizes the results of similarity indices.

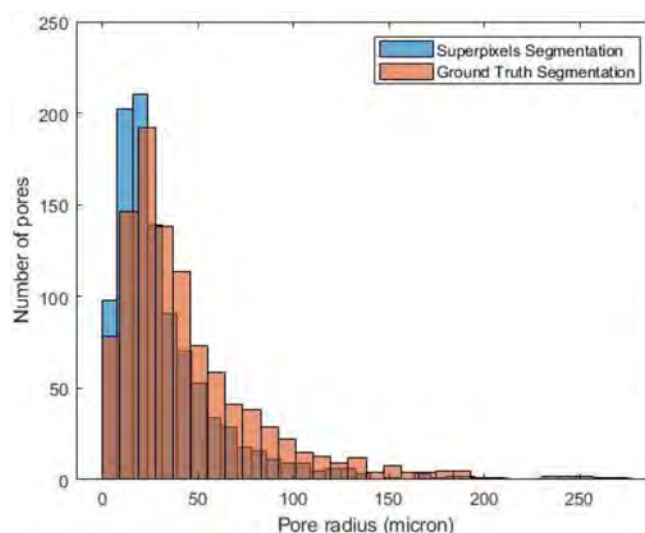


Figure 6—Pore size distribution of superpixel segmentation image and the ground truth segmented SEM image

Measurements of Physical Properties Results. Physical properties are the end-product of a typical microCT workflow. They are a very good measure to assess any segmentation process. Table 3 shows the calculations of volume fractions of the porosity phase, low-density phase, and high-density phase.

Table 3—Summary of volume fraction calculations of 2D framework

Phase	K-means		Agglomerative		GMM		Final Voting		GT
	Value	Error	Value	Error	Value	Error	Value	Error	
Porosity	0.2901	18%	0.2489	1%	0.2994	22%	0.2811	15%	0.2454
Low-density Minerals	0.6641	8%	0.7112	2%	0.5809	20%	0.6661	8%	0.7234
High-density Minerals	0.0458	47%	0.0399	28%	0.1196	283%	0.0458	47%	0.0312

We can observe that the agglomerative clustering produces the most accurate porosity estimation compared to other clustering techniques while GMM produces the highest error in quantifying the high-density mineral phase. In general, the final voting clustering produced acceptable porosity estimation. Figure 6 shows the pore size distribution of the superpixel segmented X-ray image compared to the ground truth segmented SEM image. The trend of both histograms shows high similarity with an intersection of 84.3% although we see the discrepancy in the count of the small radius pores as the superpixel algorithm identified a higher number of pore spaces with small pore radii.

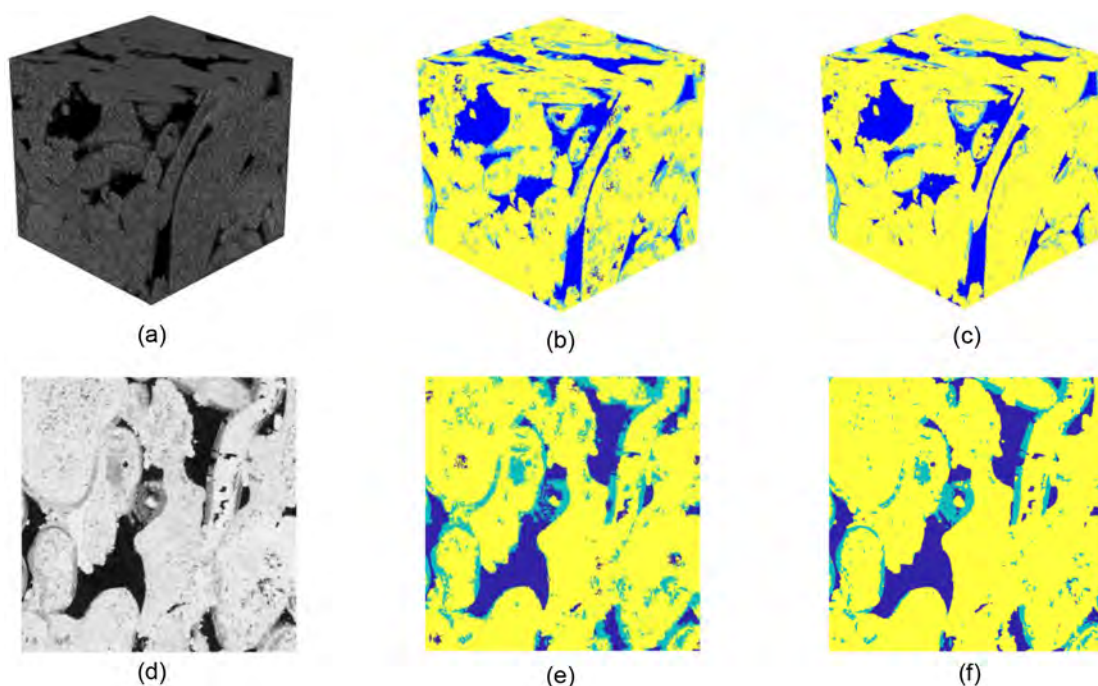


Figure 7—(a) 512^3 voxels micro-CT Indiana Limestone image; (b) 512^3 voxels supervoxel segmentation image; (c) 512^3 voxels Watershed segmentation image; (d) 2D slice of the Indiana Limestone image; (e) 2D slice of the supervoxel segmentation image; (f) 2D slice of the Watershed segmentation image

3D Application. To test the applicability of our proposed workflow on 3D images, we applied the workflow on a 512^3 image of Indiana Limestone sample and tested the results against a watershed segmentation aided by MICP obtained using Avizo software. To generate the supervoxel segmentation, we set the supervoxel size to 50 voxels which resulted in creating 54,610 segments that are equivalent to 0.04 % of the image size. Each segment was utilized to extract statistical features from its intensities' values. Figure 7 shows a 3D representation and a slice view of the raw image along with its segmentation images.

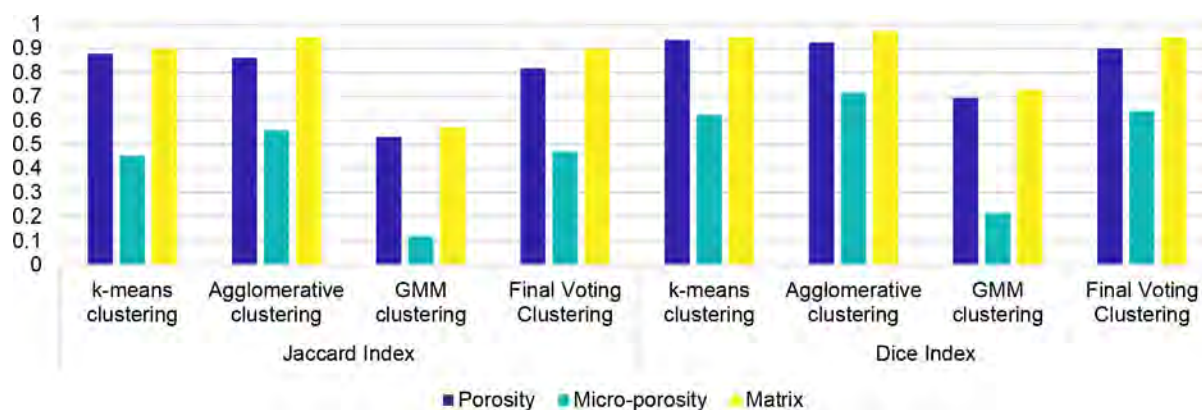


Figure 8—Summary of similarity indices results of 3D framework

Segmentation Metrics Accuracy Results. Similarity indices scores were relatively higher than the 2D application results as here we are comparing our framework to a watershed segmentation utilizing the same imaging technique and the same resolution ($5.3 \mu\text{m}$). However, this is achieved while utilizing only 0.04% of the image size to produce the segmented image. Supervoxel segmentation resulted in an average Jaccard score of 74%, and an average Dice index score of 83%. Among all the segmented phases, the error in the identification of micro-porosity was the highest. This is probably because how supervoxel boundaries don't conform with micro-porosity regions identified in the watershed segmentation. Also, micro-porosity often exists as discrete regions much smaller than supervoxel sizes, hence, increasing the error. A possible solution to this issue is refining supervoxels with high-intensity variations in a way that captures regions with distinct features.

Furthermore, similar to the 2D case, agglomerative clustering resulted in high similarity indices scores and accurate segmentation, suggesting its power in capturing spatial information as opposed to GMM models where likely more data is needed to improve the overall performance. Figure 8 shows a summary of the similarity indices results.

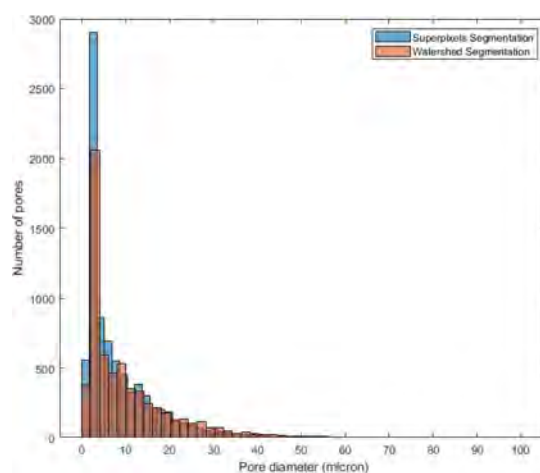


Figure 9—Pore size distribution of supervoxel segmented image and the watershed segmented image

Measurements of Physical Properties Results. Three physical properties were calculated to assess segmentation accuracy: (1) volume fractions, (2) pore size distribution, and (3) absolute permeability. Table 4 shows the volume fractions calculations where it was found that *k*-means clustering produced the most accurate porosity estimation while GMM clustering produced the least accurate result.

Table 4—Summary of volume fraction calculations of 3D framework

Phase	K-means		Agglomerative		GMM		Final Voting		WS
	Value	Error	Value	Error	Value	Error	Value	Error	
Resolved porosity	0.0949	2%	0.0818	12%	0.1732	87%	0.1029	11%	0.0928
Micro-porosity	0.1565	86%	0.1098	30%	0.3567	323%	0.1485	76%	0.0843
Solid	0.7486	9%	0.8084	2%	0.4701	43%	0.7486	9%	0.8229

Figure 9 shows the pore size distribution of both the porosity and micro-porosity in the supervoxel segmented 3D image and the watershed segmented 3D image. The distribution has the same general trend and show good agreement with an intersection of 80.6%. However, supervoxel segmentation shows more porosity and micro-porosity.

For absolute permeability calculations, both resolved porosity and micro-porosity were included while assigning a conductivity of $1.25 \times 10^{-13} \text{ m}^2$ to the micro-porosity phase. Absolute permeability calculations are presented in **Table 5**. Results along Z-direction (i.e., vertical direction) were off by around 15% while preserving the same level of accuracy using all clustering techniques presented. Generally, supervoxel segmentation resulted in lower absolute permeability which agrees with the calculations of the higher number of pores with small pore radii as illustrated in **Figure 9**.

Table 5—Summary of permeability calculations in millidarcy (mD)

Direction	K-means		Agglomerative		GMM		Final Voting		WS
	Value	Error	Value	Error	Value	Error	Value	Error	
X-direction	382.7	8%	467	12%	512	23%	387.6	7%	415.7
Y-direction	6.8	46%	10.5	17%	9.92	21%	6.9	45%	12.6
Z-direction	924.6	16%	940	14%	1241	13%	935.6	15%	1096.3

All results show the advantage of the SLIC algorithm in the over-segmentation process and highlight its ability in identifying distinct features in pore-scale images. However, some limitations of the workflow can be further improved such as the selection of the number of segments. The number of segments selection is prone to the user's input. Further development of the framework can benefit from automating the choice of the number of segments based on the image resolution, image size, and the smallest identified pore radius. Another finding from this study is the strength of the agglomerative clustering algorithm in the classification as it was able to produce the best results in both the 2D and the 3D applications. However, utilizing agglomerative clustering is a trade-off with the accuracy in the generated number of segments. Agglomerative clustering algorithm has GPU limitations, and it can only handle a limited number of generated superpixels/supervoxels. Therefore, the results were limited to a maximum number of superpixels/supervoxels. To utilize a small number of segments while preserving the finest details in an image, [Ji et al. \(2014\)](#) suggested generating superpixels and then over-segment pixels that exceed a certain threshold of variance of the constituents in each superpixel. However, user choice of the variance threshold is still a drawback of this strategy.

Conclusions

This paper presented an application of superpixels/supervoxels over-segmentation methods to segment micro-CT grayscale images of rocks. A segmentation workflow was proposed to showcase the capability of SLIC superpixels/supervoxels algorithms in obtaining statistical features from raw images that can be used to generate accurate segmentation results. In general, the framework reduces the computational cost for

segmentation compared to applying clustering techniques directly to the image. The proposed workflow was tested against segmentation obtained from SEM image of North Sea sandstone and quantitatively compared to a watershed segmented volume of 512³ Indiana Limestone sample. The results of the comparison presented in Table 6 were promising.

Table 6—Summary of comparison results

	2D North Sea Sandstone	3D Indiana Limestone Carbonate
Mean Jaccard Index	70%	73%
Mean Dice Index	81%	83%
Resolved Porosity error%	15%	11%

Future work and improvement to the workflow will focus on automating the choice of the number of superpixels/supervoxels, utilizing other statistical features such as Local Binary Pattern descriptors or Wavelet statistical applications, utilizing more unsupervised clustering techniques such as Affinity Propagation or Density-Based Spatial Clustering of Applications with Noise (DBSCAN), and improving the voting policy by selecting the clustering technique with the highest similarity coefficient rather than the statistical mode for classification.

Acknowledgements

Hussain Alqahtani acknowledges the graduate fellowship provided by Saudi Aramco. Authors acknowledge the University of New South Wales Tyree X-ray imaging facility for providing the required digital images for this paper.

References

- Achanta, R., Shaji, A., Smith, K., Lucchi, A., Fua, P., & Susstrunk, S. (2010). SLIC Superpixels. *EPFL Technical Report 149300*, June, 15. <https://doi.org/10.1109/TPAMI.2012.120>
- Achanta, R., Shaji, A., Smith, K., Lucchi, A., Fua, P., & Süssstrunk, S. (2012). SLIC Superpixels compared to state-of-the-art superpixel methods. *IEEE Transactions on Pattern Analysis and Machine Intelligence*, **34**(11), 2274–2281. <https://doi.org/10.1109/TPAMI.2012.120>
- Alqahtani, N., Chung, T., Wang, Y. Da, Armstrong, R., Swietojanski, P., & Mostaghimi, P. (2021). Flow-Based Characterization of Digital Rock Images Using Deep Learning. *SPE Journal*, 1–12. <https://doi.org/10.2118/205376-PA>
- Alqahtani, N., Mostaghimi, P., & Armstrong, R. (2021 May 19). A Multi-Resolution Complex Carbonates Micro-CT Dataset (MRCCM). Retrieved March 13, 2021, from www.digitalrockportal.org
- Boas, F. E., & Fleischmann, D. (2012). CT artifacts: Causes and reduction techniques. *Imaging in Medicine*, **4**(2), 229–240. <https://doi.org/10.2217/iim.12.13>
- Chauhan, S., Rühaak, W., Khan, F., Enzmann, F., Mielke, P., Kersten, M., & Sass, I. (2016). Processing of rock core microtomography images: Using seven different machine learning algorithms. *Computers and Geosciences*, **86**, 120–128. <https://doi.org/10.1016/j.cageo.2015.10.013>
- Chung, T., Wang, Y. D., Armstrong, R. T., & Mostaghimi, P. (2019). Approximating permeability of microcomputed-tomography images using elliptic flow equations. *SPE Journal*, **24**(3), 1154–1163. <https://doi.org/10.2118/191379-PA>
- Comaniciu, D., & Meer, P. (2002). Mean shift: A robust approach toward feature space analysis. *IEEE Transactions on Pattern Analysis and Machine Intelligence*, **24**(5), 603–619. <https://doi.org/10.1109/34.1000236>
- Cortina-Januchs, M. G., Quintanilla-Dominguez, J., Vega-Corona, A., Tarquis, A. M., & Andina, D. (2011). Detection of pore space in CT soil images using artificial neural networks. *Biogeosciences*, **8**(2), 279–288. <https://doi.org/10.5194/bg-8-279-2011>
- Demuth, H., & Beale, M. (2000). Neural Network Toolbox for use with MATLAB. 9.
- Dinç, İ., Dinç, S., Sigdel, M., Sigdel, M. S., Aygün, R. S., & Pusey, M. L. (2015). Chapter 12 – DT-Binarize: A decision tree based binarization for protein crystal images (L. Deligiannidis & H. R. B. T.-E. T. in I. P. Arabnia Computer Vision and Pattern Recognition (eds.); pp. 183–199). Morgan Kaufmann. <https://doi.org/10.1016/B978-0-12-802045-6.00012-0>

- Gostick, J., Khan, Z., Tranter, T., Kok, M., Agnaou, M., Sadeghi, M., & Jervis, R. (2019). PoreSpy: A Python Toolkit for Quantitative Analysis of Porous Media Images. *Journal of Open Source Software*, **4**(37), 1296. <https://doi.org/10.21105/joss.01296>
- Grachev, N. E. (2012). Digital core analysis - the future of petrophysics. In SPE Russian Oil and Gas Exploration and Production Technical Conference and Exhibition (p. 3). *Society of Petroleum Engineers*. <https://doi.org/10.2118/160499-MS>
- Hapca, S.M., Houston, A.N., & Baveye, P.C. (2013) New Local Thresholding Method for Soil Images by Minimizing Grayscale Intra-Class Variance. *Vadose Zone Journal*, **12**(3), vzj2012.0172. <https://doi.org/10.2136/vzj2012.0172>
- Hoiem, D., Efros, A.A., & Hebert, M. (2005). Automatic photo pop-up. *ACM Transactions on Graphics*, **24**(3), 577–584. <https://doi.org/10.1145/1073204.1073232>
- Jaccard, P. (1912.) THE DISTRIBUTION OF THE FLORA IN THE ALPINE ZONE.1. *New Phytologist*, **11**(2), 37–50. <https://doi.org/https://doi.org/10.1111/j.1469-8137.1912.tb05611.x>
- Ji, S., Wei, B., Yu, Z., Yang, G., – Yin, Y. (2014). A new multistage medical segmentation method based on superpixel and fuzzy clustering. *Computational and Mathematical Methods in Medicine*, 2014. <https://doi.org/10.1155/2014/747549>
- Ketcham, R.A., & Carlson, W.D. (2001). Acquisition, optimization and interpretation of x-ray computed tomographic imagery: Applications to the geosciences. *Computers and Geosciences*, **27**(4), 381–400. [https://doi.org/10.1016/S0098-3004\(00\)00116-3](https://doi.org/10.1016/S0098-3004(00)00116-3)
- Kjellsen, K., MonsØy, A., Isachsen, K., & Detwiler, R.J. (2003). Preparation of Flat-Polished Specimen for SEM-Backscattered Electron Imaging and X-Ray Microanalysis—Importance of Epoxy Impregnation. *Cement and Concrete Research*, **33**, 611–616. [https://doi.org/10.1016/S0008-8846\(02\)01029-3](https://doi.org/10.1016/S0008-8846(02)01029-3)
- Leu, J.-G. (1992). mage contrast enhancement based on the intensities of edge pixels. *CVGIP: Graphical Models and Image Processing*, **54**(6), 497–506. [https://doi.org/https://doi.org/10.1016/1049-9652\(92\)90069-A](https://doi.org/https://doi.org/10.1016/1049-9652(92)90069-A)
- Leu, L., Berg, S., Enzmann, F., Armstrong, R.T., & Kersten, M. (2014). Fast X-ray Micro-Tomography of Multiphase Flow in Berea Sandstone: A Sensitivity Study on Image Processing. *Transport in Porous Media*, **105**(2), 451–469. <https://doi.org/10.1007/s11242-014-0378-4>
- Lin, Q., Al-Khulaifi, Y., Blunt, M.J., & Bijeljic, B. (2016). Quantification of sub-resolution porosity in carbonate rocks by applying high-salinity contrast brine using X-ray microtomography differential imaging. *Advances in Water Resources*, **96**, 306–322. <https://doi.org/10.1016/j.advwatres.2016.08.002>
- Malik, J., Kiranyaz, S., Al-Raoush, R.I., Monga, O., Garnier, P., Fofou, S., Bouras, A., Iosifidis, A., Gabbouj, M., & Baveye, P.C. (2018). 3D Quantum Cuts for Automatic Segmentation of Porous Media in Tomography Images. *Under Review in IEEE TPAMI*, 1–11.
- Mičušik, B., & Košecká, J. (2009). Semantic segmentation of street scenes by superpixel co-occurrence and 3D geometry. *2009 IEEE 12th International Conference on Computer Vision Workshops, ICCV Workshops 2009*, 625–632. <https://doi.org/10.1109/ICCVW.2009.5457645>
- Neubert, P. (2015). *Superpixels and their Application for Visual Place Recognition in Changing Environments*.
- Niu, Y., Mostaghimi, P., Shabaninejad, M., Swietojanski, P., –Armstrong, R. (2020). Digital Rock Segmentation for Petrophysical Analysis With Reduced User Bias Using Convolutional Neural Networks. *Water Resources Research*, **56**. <https://doi.org/10.1029/2019WR026597>
- Oh, W., & Brent Lindquist, W. (1999). Image thresholding by indicator kriging. *IEEE Transactions on Pattern Analysis and Machine Intelligence*, **21**(7), 590–602. <https://doi.org/10.1109/34.777370>
- Olaode, A., Naghdy, G., & Todd, C. (2014). Unsupervised Classification of Images: A Review. *International Journal of Image Processing*, **8**, 2014–2325.
- Otsu, N. (1979). A Threshold Selection Method from Gray-Level Histograms. *IEEE Transactions on Systems, Man, and Cybernetics*, **9**(1), 62–66. <https://doi.org/10.1109/TSMC.1979.4310076>
- Pitas, I., & Venetsanopoulos, A.N. (1986). Nonlinear order statistic filters for image filtering and edge detection. *Signal Processing*, **10**(4), 395–413. [https://doi.org/10.1016/0165-1684\(86\)90047-2](https://doi.org/10.1016/0165-1684(86)90047-2)
- Pont-Tuset, J., Arbelaez, P., Barron, J., Marques, F., Malik, J. (2015). Multiscale Combinatorial Grouping for Image Segmentation and Object Proposal Generation. *IEEE Transactions on Pattern Analysis and Machine Intelligence*, **39**. <https://doi.org/10.1109/TPAMI.2016.2537320>
- Scott, G. (2020, January 16). North Sea Sandstone SEM Images. Retrieved February25, 2021, from www.digitalrockportal.org
- Sheppard, A.P., Sok, R.M., & Averdunk, H. (2004). Techniques for image enhancement and segmentation of tomographic images of porous materials. *Physica A: Statistical Mechanics and Its Applications*, **339**(1–2), 145–151. <https://doi.org/10.1016/j.physa.2004.03.057>
- Shi, J.–, Malik, J. (2000). Normalized cuts and image segmentation. *IEEE Transactions on Pattern Analysis and Machine Intelligence*, **22**(8), 888–905. <https://doi.org/10.1109/34.868688>

- Smith, M.M., Sholokhova, Y., Hao, Y., & Carroll, S.A. (2013). CO₂-induced dissolution of low permeability carbonates. Part I: Characterization and experiments. *Advances in Water Resources*, **62**, 370–387. <https://doi.org/10.1016/j.advwatres.2013.09.008>
- Sorensen, T.J. (1948). *A method of establishing groups of equal amplitude in plant sociology based on similarity of species content and its application to analyses of the vegetation on Danish commons*. I kommission hos E. Munksgaard.
- Soulaine, C., Gjetvaj, F., Garing, C., Roman, S., Russian, A., Gouze, P., & Tchelepi, H. A. (2016). The Impact of Sub-Resolution Porosity of X-ray Microtomography Images on the Permeability. *Transport in Porous Media*, **113**(1), 227–243. <https://doi.org/10.1007/s11242-016-0690-2>
- Srivastava, R.G. and N. (2007). Mixture models. *The Journal of International Trade and Diplomacy*, **1**(2), 159–202. http://link.springer.com/10.1007/978-3-642-19318-7_53
- Uijlings, J.R., Sande van de, K.E., Gevers, T. & Smeulders, A.W.M. (2013). Selective Search for Object Recognition. *International Journal of Computer Vision*, **104**(2), 154–171.
- Verri, I., Della Torre, A., Montenegro, G., Onorati, A., Duca, S., Mora, C.A., Radaelli, F., Trombin, G., (2017). Development of a Digital Rock Physics workflow for the analysis of sandstones and tight rocks. *Journal of Petroleum Science and Engineering*, **156**(April), 790–800. <https://doi.org/10.1016/j.petrol.2017.06.053>
- Vogel, H.J., & Kretschmar, A. (1996). Topological characterization of pore space in soil - Sample preparation and digital image-processing. *Geoderma*, **73**(1–2), 23–38. [https://doi.org/10.1016/0016-7061\(96\)00043-2](https://doi.org/10.1016/0016-7061(96)00043-2)
- Wang, W., Kravchenko, A.N., Smucker, A.J.M. & Rivers M.L., (2011). Comparison of image segmentation methods in simulated 2D and 3D microtomographic images of soil aggregates. *Geoderma*, **162**(3–4), 231–241. <https://doi.org/10.1016/j.geoderma.2011.01.006>
- Ward, J.H. (1963). Hierarchical Grouping to Optimize an Objective Function. *Journal of the American Statistical Association*, **58**(301), 236–244. <https://doi.org/10.1080/01621459.1963.10500845>